Contents lists available at ScienceDirect

# Corrosion Science

# The cathodic behaviour of Al–Mn precipitates during atmospheric and saline aqueous corrosion of a sand-cast AM50 alloy

Mohsen Danaie [a],*, Robert Matthew Asmussen [b], Pellumb Jakupi [b], David W. Shoesmith [b], Gianluigi A. Botton [a]

[a] Department of Materials Science and Engineering, Brockhouse Institute for Materials Research and Canadian Centre for Electron Microscopy, McMaster University, Hamilton, Ontario, Canada
[b] Department of Chemistry and Surface Science Western, Western University, London, Ontario, Canada

## ARTICLE INFO

## ABSTRACT

The behaviour of Al–Mn precipitates during atmospheric and aqueous corrosion of an AM50 Mg alloy was investigated using site-specific analytical electron microscopy. After air-exposure, localized attack was observed close to Al–Mn precipitates, with the top layer of the intermetallic enriched in Al and O. During immersed corrosion, these precipitates developed protruding domes of corrosion products, with crystalline $Mg(OH)_2$ on top and an inner layer of crystalline MgO. After prolonged immersion, these precipitates showed evidence of preferential Al dissolution, ultimately developing a fragmented interlayer of $Mn_3O_4$. This phase transformation is linked to the enhanced hydrogen evolution rates adjacent to these precipitates.

## 1. Introduction

Magnesium alloys with high strength-to-weight ratio, good castability and machinability are desirable candidate materials for automotive and aerospace applications. The major hindrance to their wider application is their susceptibility to corrosion, especially in chloride-containing aqueous environments [1]. The porosity, poor adhesion, and a narrow pH range of stability of the corrosion product (generally $Mg(OH)_2$), combined with the high electrochemical anodic activity of pure Mg results in high corrosion rates [2]. Since Mg is so anodically reactive, its corrosion can be exacerbated when the generally α-Mg matrix contains more noble secondary phases to which it can galvanically couple. Such phases are commonly incorporated in the matrix to enhance the mechanical properties of the alloy [3–5]. The presence of impurities such as Ni, Cu, and Fe can also enhance the anodic reactivity and the influence of microgalvanic coupling upon it [5,6].

The role of alloying elements is critical in optimizing the corrosion properties of Mg alloys. Addition of Mn has long been known to enhance the corrosion resistance of cast Mg alloys by capturing the residual Fe during casting [7,8]. A secondary advantage of adding Mn is grain refinement [9–11]. In the absence of Fe, numerous intermetallic phases are possible in the Al–Mn system [12]. In the

Mg-rich Mg–Al–Mn ($0 \leqslant Mn$ (wt.%) $\leqslant 3$ and $0 \leqslant Al$ (wt.%) $\leqslant 15$) system it has been demonstrated, both experimentally [13] and theoretically [14], that in the melt temperature range (700–750 °C) the equilibrium phases are β-Mn (Cubic) and $Al_8Mn_5$ (rhombohedral). Since their atomic radii are almost equal, Fe can replace Mn in the latter phase to form the substitutional solid solution phase, $Al_8(Mn,Fe)_5$ [9].

Electrochemical measurements have shown that the Al–Mn intermetallics are cathodic with respect to the α-Mg matrix [3,15–17] (but less so than the Fe impurities that Mn is meant to capture). The eutectic intermetallic β-$Mg_{17}Al_{12}$ phase has been shown to be also weakly cathodic with respect to the α-Mg matrix [18–22], but can form a passive layer which results in an overall improvement in corrosion resistance provided that this phase is present in a continuous and uniform network [17,19,23]. The α-Mg grains themselves will have different potentials depending on the amount of Al in solid solution, with more Al resulting in slightly more noble potentials [16,24–27]. According to Mathieu et al. [16], the corrosion potential of α-Mg increases linearly, from $-1.55 \ V_{SCE}$ for pure Mg to $-1.40 \ V_{SCE}$ for α-Mg containing 9 at.% Al. The lowered corrosion rates of Al-rich α-Mg grains has been linked to accumulation of $Al^{3+}$ entities on the surface [28–30], percolation of amorphous $Al_2O_3$ within the $MgO/Mg(OH)_2$ corrosion layer [31], and most recently shown by the present authors [32,33], to the development of a metallic Al-rich layer at the metal/corrosion layer interface.

* Corresponding author. Tel.: +1 905 525 9140x24862; fax: +1 905 521 2773.
E-mail addresses: danaiem@mcmaster.ca (M. Danaie), gbotton@mcmaster.ca (G.A. Botton).

**Table 1**
Composition of the AM50 magnesium alloy used for this study.

| Major elements (wt.%) | | | | Minor elements (ppm-weight) | | | | |
|---|---|---|---|---|---|---|---|---|
| Al | Mn | Zn | Si | P | Cu | Fe | Ni | Cr |
| 4.42 | 0.29 | 0.09 | 0.02 | 56 | 23 | 8 | 4 | 3 |

In a recently proposed mechanism, based on scanning vibrating electrode measurements, Williams et al. [34] suggested a higher population of Al–Mn precipitates left in the wake of an advancing anode as the source of cathodic activity on a corroding AZ31 surface in aqueous NaCl solution. These intermetallics were also shown to coincide with the localized damage on a corroded AZ31 surface in a salt-fog environment [17]. Despite these studies, little is known about the chemical and microstructural state of these Al–Mn phases during corrosion. Recently [32], we performed site-specific analytical electron microscopy to study the microstructure of the corroded sand-cast AM50 alloy, focusing on the role of Al distribution and its effect on local corrosion behaviour. The current study applies the same experimental methodology to the Al–Mn precipitates to further understand the sequence of events occurring during the corrosion of the AM50 alloy.

## 2. Experimental procedure

Sand-cast AM50 alloy specimens were provided by General Motors (Canada) in the form of cylindrical ingots. The chemical composition of this alloy is presented in Table 1, and complies with the ASTM B275 standard for this alloy [35]. A detailed description of the procedures used for surface preparation and microstructural characterization of the alloy in the pristine state has been published previously [32].

Specimens were corroded in 1.6 wt.% NaCl (reagent grade, 99% assay) solution made with high purity water (HPLC grade). The sample was immersed for two periods (18 and 96 h) and then removed from the solution, washed with anhydrous ethanol and dried. Site-specific transmission electron microscopy (TEM) specimens were then prepared using the standard *in-situ* lift-out technique in a focused ion beam (FIB-Zeiss NVision 40, equipped with an X-ray energy-dispersive spectrometer XEDS – Oxford, Inca, Silicon drift detector). FIB specimens were prepared from the Al–Mn precipitates at various stages of corrosion. A specimen was also prepared from an air-exposed sample for comparison (7 days exposure to laboratory air with relative humidity between 28% and 35%). The FIB was also used in scanning electron microscopy (SEM) mode to characterize the initial microstructure.

Microscopic characterization of the FIB specimens was performed with an FEI Titan 80–300 (scanning) transmission electron microscope, (S)TEM, equipped with a Gatan Image Filter (GIF) electron energy-loss spectrometer (EELS), and an X-ray energy-dispersive spectrometer (XEDS-Oxford, Inca, Si(Li) detector). The accelerating voltage was set at 300 kV. The energy spread of the primary electron beam, measured at the full-width-at-half-maximum of the zero-loss peak in vacuum was 0.7 eV or better. In order to minimize electron beam damage, all electron microscopy characterization was performed using a cryogenically cooled sample stage (*T* = 95 K). Details of the electron microscopy and
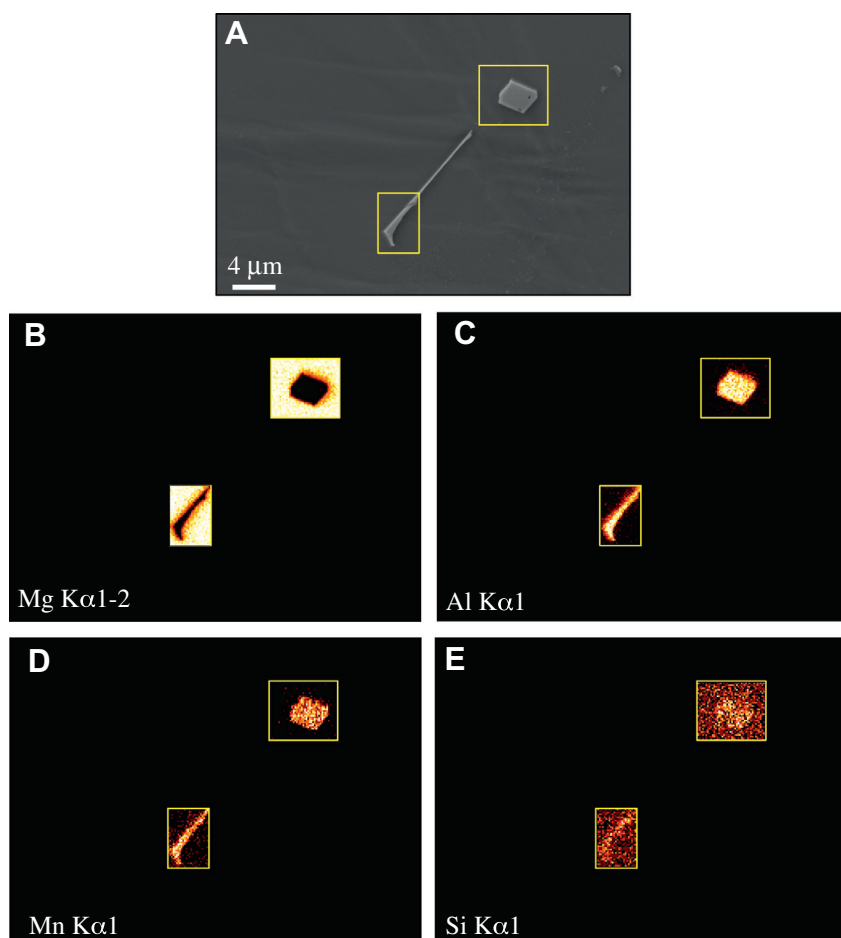


**Fig. 1.** (A) Area containing two edged precipitates, (B) thorough (E) XEDS elemental maps of Mg, Al, Mn, and Si of two select regions of area shown in (A).

spectroscopy techniques applied have been published in a recent publication [32].

# 3. Results

## 3.1. Air-exposed state of the Al–Mn precipitate

The Al–Mn precipitates in the sand-cast AM50 alloy form at relatively high temperatures, e.g. $Al_8Mn_5$ can form at around 1000 °C [14]. Hence, these precipitates are among the first solid phases formed during casting of Mg alloys. The melt temperature during casting, depending on the casting method, can be 650–760 °C [36]. As observed in the SEM micrographs of the as-polished sand-cast AM50 alloy, Fig. 1(A), this results in sharp-edged shapes in these precipitates. The XEDS maps, Fig. 1(B–E), show that, beside Mn and Al, there is a contribution from Si in some of these precipitates.

To further investigate the Al–Mn precipitates in the polished and air-exposed state, TEM analysis was performed on a specimen prepared by FIB. The area investigated is shown in the SEM micrograph in Fig. 2(A). Exposure to laboratory air for 7 days after polishing leads to significant localized corrosion damage in the vicinity of the Al–Mn intermetallic particle (indicated by the red arrow on Fig. 2(A)). The FIB sample prepared from this particle was imaged using a STEM high-angle annular dark field (HAADF) detector, Fig. 2(B). A selected area diffraction pattern (SAD) of this Al–Mn intermetallic, Fig. 2(C), can be indexed as $Al_8Mn_5$ (SAD simulation shown in Fig. 2(D), using available crystallographic information [9,37]). The elemental quantification with XEDS (data shown in Fig. 3(D)) confirms the Al:Mn atomic ratio of 1.17, which is within the reported range for the non-stoichiometric intermetallic phase "$Al_8Mn_5$" (Al:Mn nominal

ratio: 1.62–1.13) [14]. XEDS point analyses close to the air-exposed surface detected a 5–13% increase in the Al/(Al + Mn) ratio, with respect to the bulk ratio (Fig. 3, panels C and D). This superficial "Al-rich" region also coincides with higher O contents.

The two domains adjacent to the Al–Mn intermetallic phase, indicated by the green arrow in Fig. 2(B), are artifacts produced during the casting process. XEDS measurements show that the phase indicated by the arrow is rich in F and Mg, with a ratio close to that of $MgF_2$. The porous region surrounding $MgF_2$, and neighbouring $Al_8Mn_5$ is a mixture of Mg and MgO. The $MgF_2$ is most likely formed from the reaction of the Mg melt with the cover gas (mixture of $CO_2$ and $SF_6$) during casting, as also reported in the literature [8,38,39].

## 3.2. Corroded state of the Al–Mn precipitates (18-h immersion)

The morphology of the AM50 alloy surface surrounding the Al–Mn precipitates after 18 h of immersion in 1.6 wt.% NaCl solution is presented in Fig. 4. Some of the Al–Mn intermetallic particles develop domes of corrosion product (marked with red arrows in panels A, B, and C) while others, with more elongated shapes appear to be less active with smaller amounts of accumulated corrosion products (green arrows in panels C and D of Fig. 4). The corrosion product dome and its formation will be addressed in the next section, based on experiments with a longer immersion time (96 h).

To further characterize the needle-like Al–Mn intermetallic particles, the elongated particle marked in Fig. 4(C) was extracted via the standard FIB lift-out technique. A selected area electron diffraction pattern from the particle can be indexed as $Al_8Mn_5$ (data presented in the supplementary section, Fig. S.1). In contrast to the
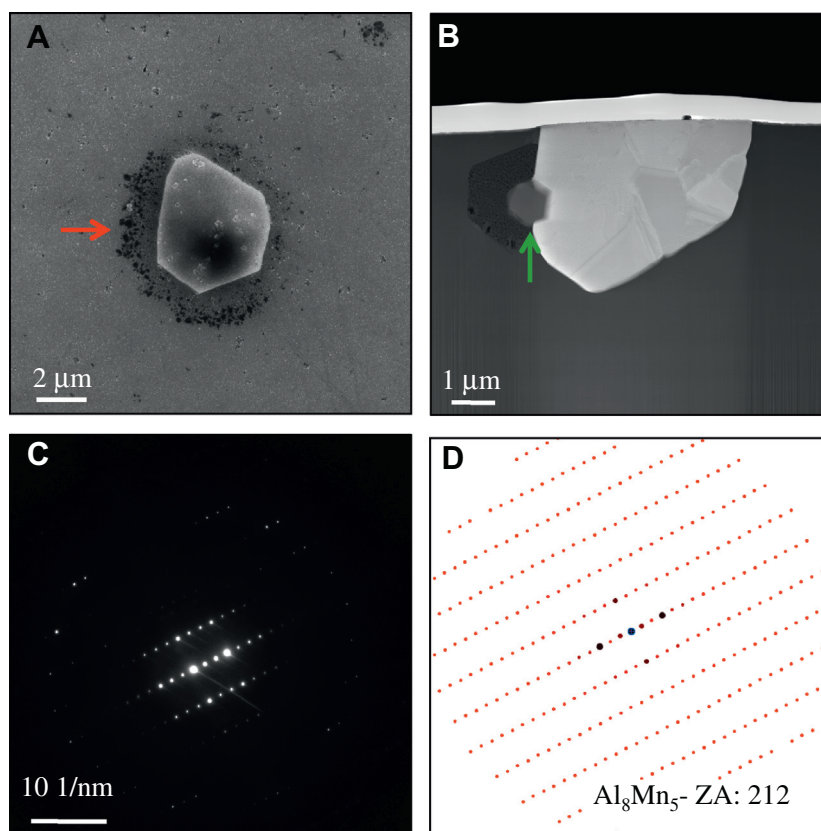


**Fig. 2.** (A) A polished and air-exposed Al–Mn intermetallic chosen for analytical electron microscopy (SEM micrograph). Red arrow points to localized corrosion damage. (B) STEM HAADF image showing the FIB sample prepared from the intermetallic phase shown in (A). Green arrow marks the $MgF_2$ particle (casting artifact). The phase marked by the green arrow is rich in F. (C) Selected area electron diffraction pattern of the Al–Mn intermetallic. (D) Simulated diffraction pattern. (For interpretation of the references to colour in this figure legend, the reader is referred to the web version of this article.)
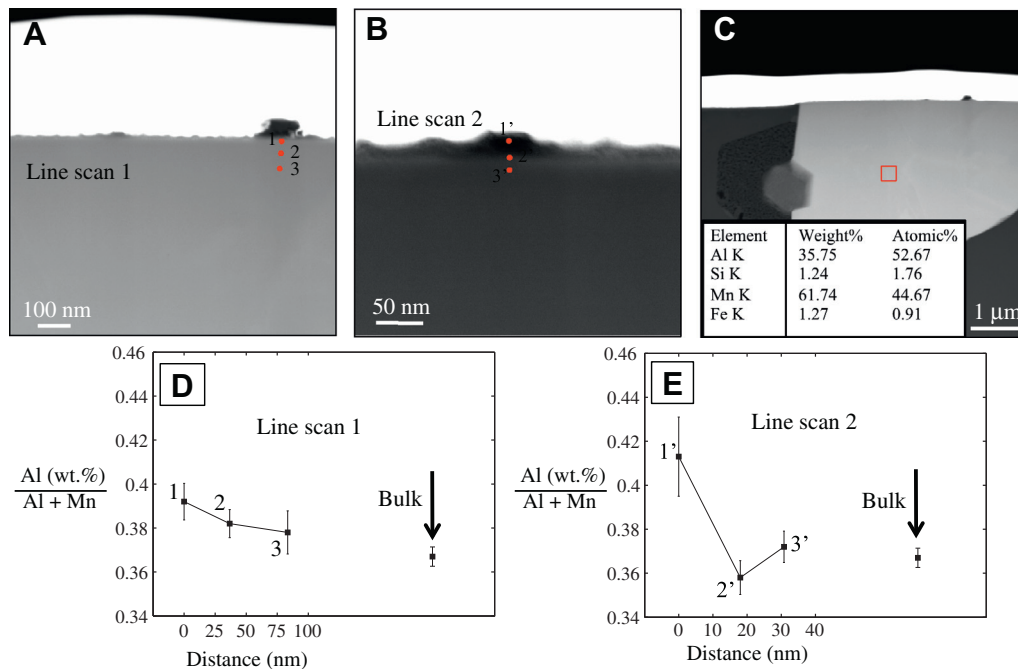
**Fig. 3.** (A and B) STEM HAADF images from the surface of the air-exposed $Al_8Mn_5$ intermetallic phase, with the positions of the two XEDS line scans marked. (C) XEDS elemental analysis of the bulk of the intermetallic. The composition presented in the table corresponds to the region marked in the image. (D and E) Plots of the ratio Al/(Al + Mn) for the two line scans 1 and 2, respectively. The data points marked "bulk" in (D and E), provided for comparison, are acquired from the region marked in (C). The difference in distances between the data points reflect the difference in magnification. The two locations selected for XEDS line scans (A and B) were chosen in order to avoid the W protective layer on top.
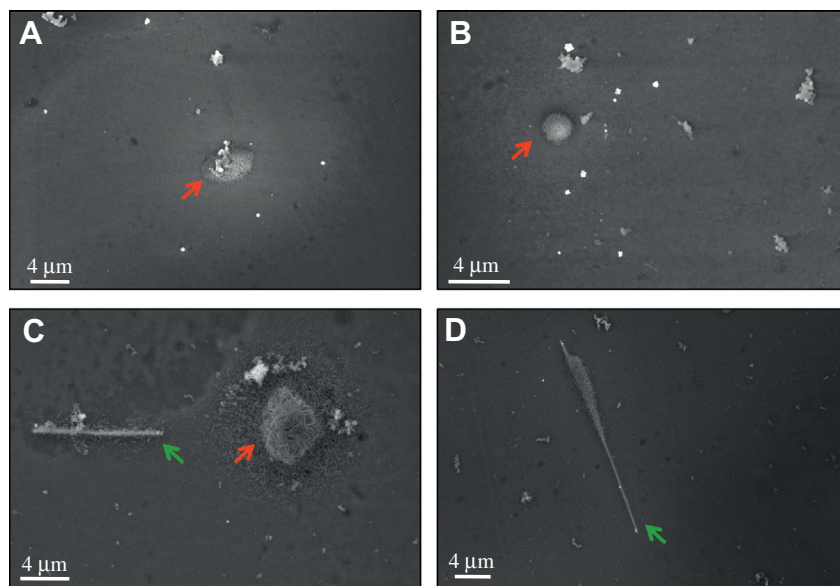


**Fig. 4.** SEM micrographs showing the surface morphology of the 18-h immersed AM50 alloy sample. Red arrows point to domes of corrosion products formed on top of Al–Mn intermetallics. Green arrows point to Al–Mn precipitates with little or no corrosion products surrounding them. The needle-shaped intermetallic particle marked in (C) was used for further FIB/TEM analyses. (For interpretation of the references to colour in this figure legend, the reader is referred to the web version of this article.)

intermetallic particle in Fig. 2, here we observed that upon bringing the intermetallic to a symmetrical zone axis (by tilting the specimen with respect to the electron beam), the Mg matrix is also close to a low-index zone axis. This indicates a crystallographic orientation relationship (OR) between the $Al_8Mn_5$ and Mg in this case (the matching direction observed here is: $[001]$-$Al_8Mn_5||[10\bar{1}2]$-Mg, which differs slightly from the predicted OR between these two phases [9]). This crystallographic relationship indicates an initially coherent or semi-coherent inter-

face between the two phases, with the needle-like shape a consequence of the thermodynamic tendency to minimize the energy cost associated with the interphase interfaces [40]. As noted in the literature [9], $Al_8Mn_5$ has few crystallographic orientations that provide a close match to that of the matrix Mg, and hence it is a relatively poor grain refiner [10,11]. It is not expected that the presence or absence of an OR with Mg would alter the electro-chemical activity of the $Al_8Mn_5$ intermetallic particle. The lesser extent of corrosion activity in the vicinity of the semi-coherent,
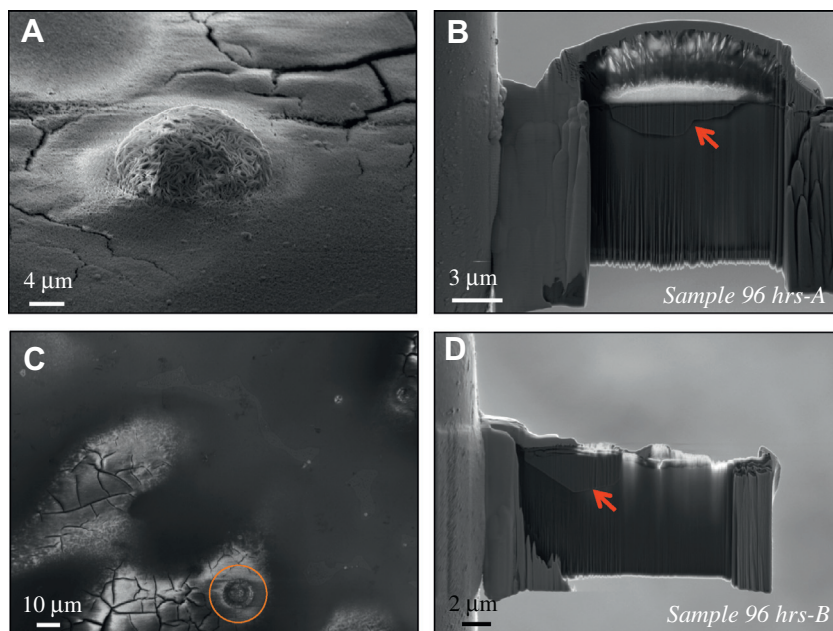
**Fig. 5.** (A and C) SEM micrographs showing areas of interest, close to Al–Mn intermetallics, in the 96 h corroded state. In (C) the corrosion dome appears to be broken and in (A) still attached. (B and D) FIB samples prepared from region of interests shown in (A and C), respectively. The arrows point to the intermetallic phase.

needle-shaped intermetallics is most likely associated with the smaller exposed surface area of these particles. The above assessment holds true if the anodic regions coupling to the Al–Mn precipitates are similar in composition to one another. Indeed, the Al concentration in the matrix solid solution here (sample shown in Fig. S.1) was the same as another area with the corrosion product dome (both with 2–3 wt.% Al).

### 3.3. Corroded state of the Al–Mn precipitates (96-h immersion)

Two FIB specimens of the 96 h corroded areas in the proximity of the Al–Mn precipitates were prepared: (i) from a precipitate with a dome of corrosion products attached (*Sample 96hrs-A*, panel A, Fig. 5), and (ii) from a precipitate with the corrosion products detached (*Sample 96hrs-B*, panel C, Fig. 5). Panels (B) and (D) in Fig. 5, show the prepared FIB specimens from these two areas (the arrows indicate the Al–Mn intermetallic phases in each case).

Fig. 6(A and B) shows micrographs of *Sample 96hrs-A*, with the area used for XEDS elemental mapping outlined in (B). Bright area at the top in panel (A) is the W protective layer. The intermetallic appears bright due to the larger average atomic number compared to the Mg matrix. Bright bands at the left and right in panel (A) are due to the larger thickness of the sample in those regions. A thin delaminated section is apparent on top of the intermetallic phase (marked by arrows in panels (A) and (B)). The XEDS elemental maps show that this delaminated layer yields strong Mn and O signals and is depleted in Al. The O and Mg maps indicate variations in O/Mg content within the corrosion product dome. XEDS elemental maps acquired at higher magnification, showing the delaminated layer and the elemental distribution in greater details, are presented in the supplementary section, Fig. S.2. Depletion of Al from the top segment of the intermetallic is evident in Fig. 6(E) (Also supplementary Fig. S.2(D)). A lower Si content can also be detected. Fig. S.3 in the supplementary section presents individual XEDS spectra confirming this elemental distribution, and demonstrating a weak Al signal in the region immediately above the delaminated layer and within the lower sections of the corrosion product.

Low-loss EEL spectra acquired from *Sample 96hrs-A*, Fig. 7, show that two distinct regions are present in the corrosion product dome.

Fig. 7(B) shows the EEL spectra from the marked locations in panel (A). The spectrum from the top layer (#1) shows a broad peak at 22 eV characteristic of MgO [41], and a secondary peak at 8.5 eV, which has been reported in the low-loss EEL spectrum of Mg(OH)$_2$ [42], and confirmed elsewhere [32] by reference to spectra acquired from brucite powder. This peak at 8.5 eV appears only as a shoulder in spectrum #2 acquired from the inner region of the deposit.

To determine the nature of the dark boundary between the two regions within the dome, a low-loss spectrum image was obtained from the marked area in Fig. 7(C). A plot of specimen thickness normalized by the inelastic mean free path (MFP) can be extracted from the low-loss EEL spectra [43]. The blue arrow in the micrograph in (C) shows the direction of the horizontal axis in (D). As indicated by the orange arrow, the dark boundary area has high porosity, the minimum thickness being observed at this location.

The evolution in crystal structure within the top layer of *Sample 96hrs-A* was examined by acquiring a series of SAD patterns, Fig. 8. The TEM-BF micrograph in (A) shows the starting location (1), with the arrow indicating the direction in which successive SADs were obtained. The first column to the right of (A), presents the location (TEM-BF) corresponding to the SAD patterns, with the patterns shown in the second column. The starting location (1) is within the Al–Mn precipitate, as shown in micrograph (B). Simulations of the measured SAD (B*) pattern yields a good match with the [3 2 2] zone axis of the rhombohedral phase Al$_8$Mn$_5$ (B**) (the elemental atomic ratio measured at this location was Al:Mn = 1.15, consistent with the previous measurement and with the compositional range of this phase as discussed above). The SAD pattern in panel (C) was measured in the delaminated layer on top of the precipitate, and shows (C*) diffraction rings (MgO) overlapping with the faint spots observed in (B*). The BF micrograph (D), recorded in the lower section of the protruding corrosion product dome, exhibits a needle-like morphology, and the SAD pattern (D*) (simulated in D**) can be indexed as MgO. The area shown in (E) is the thin porous band between the two regions in the dome, indicated by the red arrow in Fig. 7. The SAD pattern (E*) shows a mixed ring pattern characteristic of MgO and Mg(OH)$_2$. Above this boundary, (F), the SAD pattern (F*) shows a single phase Mg(OH)$_2$ structure [44]. This evolution in SAD patterns demon-
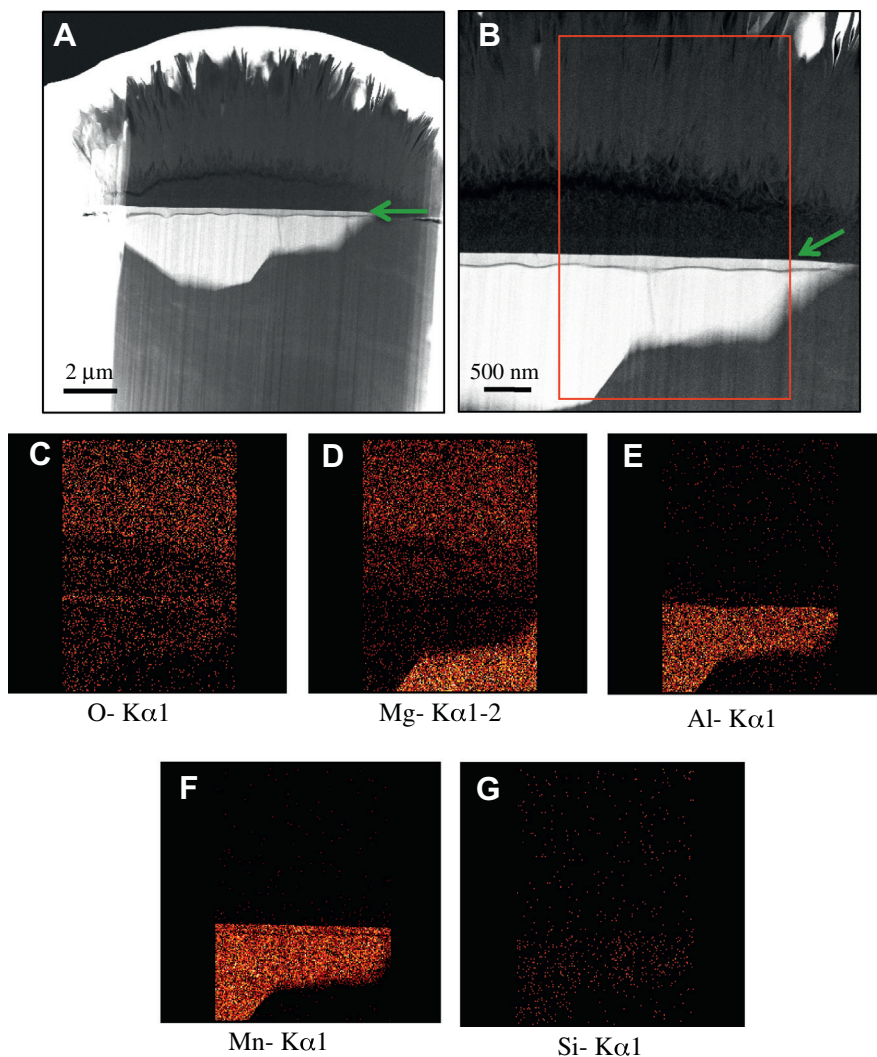
**Fig. 6.** (A) Low magnification view of *Sample 96hrs-A*. Box in (B) marks the area used for the XEDS maps. XEDS elemental maps: (C) O, (D) Mg, (E) Al, (F) Mn, (G) Si. Arrows in (A and B) point to the delaminated layer from the intermetallic phase.

strates that the inner region of the corrosion product dome is mainly MgO with an outer section of predominantly crystalline $Mg(OH)_2$. We also point out that the microstructure seems to have been well preserved throughout our sample preparation and TEM observations, given the very sharp diffraction rings and spots with no detectable amorphization.

The specimen prepared from the Al–Mn precipitate with the corrosion dome detached, *Sample 96hrs-B*, shows a severe delamination and fracture in the top segments of the particle, Fig. 9. The XEDS elemental maps demonstrate that Al is not detected in the fragmented areas, but strong Mn and O signals are observed. A series of XEDS point spectra from this region (supplementary section, Fig. S.4) confirms that the corrosion film contains some residual Al. The fractured fragments of the precipitate show strong Mn and O signals, whereas the areas between these fragments predominantly yield Mg and O signals.

A series of SAD patterns was also obtained for this area. The starting position (1) is marked in Fig. 10(A), with the arrow indicating the scan direction in which the sequence of patterns was acquired. The size of the area, from which a diffraction pattern is gathered, is comparable to that of the circle shown in (A). Panel (B) of Fig. 10 shows the pattern for the Al–Mn precipitate. A close match between the experimental SAD and the [3 2 1] zone axis of $Al_8Mn_5$ is found [9,37]. The simulation is shown in plate #1*,

Fig. 10). XEDS measurements on the intermetallic phase in Fig. 10 indicated an atomic ratio of Al:Mn = 1.13. A close match was also found with the [5 6 1] zone axis of the cubic phase $Al_{57-}Mn_{12}$ (Space group: Pm-3 (200), $a$ = 12.68 Å [45]), but this phase can be ruled out based on the XEDS atomic ratio and the literature regarding the equilibrium phases in this system [13,14].

When the area analyzed is further along the arrow, Fig. 10(A), a ring pattern gradually appears along with the $Al_8Mn_5$ spot pattern (panel #2). The ring pattern can be indexed (simulation shown in #2*) as the tetragonal $Mn_3O_4$ [46]. In patterns recorded further away from the interface fewer diffraction spots for $Mn_3O_4$ are present. For SAD #3, the 112 reflection spot of this phase is marked by the red arrow. Beyond this section (SAD #4) the ring pattern can be indexed as MgO. These electron diffraction observations correlate well with the XEDS measurements (supplementary Fig. S.4).

Low-loss EELS were also acquired in this region to determine the distribution of the phases present. The red box in Fig. 11(A) indicates the area used for spectrum imaging. Three spectra from the designated locations in (A) are plotted in panel (C). Data point #3, gathered from within the precipitate, shows that the volume plasmon for this phase ($Al_8Mn_5$) is around 17 eV. Spectrum 1 was recorded on the edge of the delaminated region above the Al–Mn precipitate, and shown to be $Mn_3O_4$ by electron diffraction, Fig. 10(B). The Mn–$M_{2,3}$ edge at 50 eV is clearly visible. Spectrum
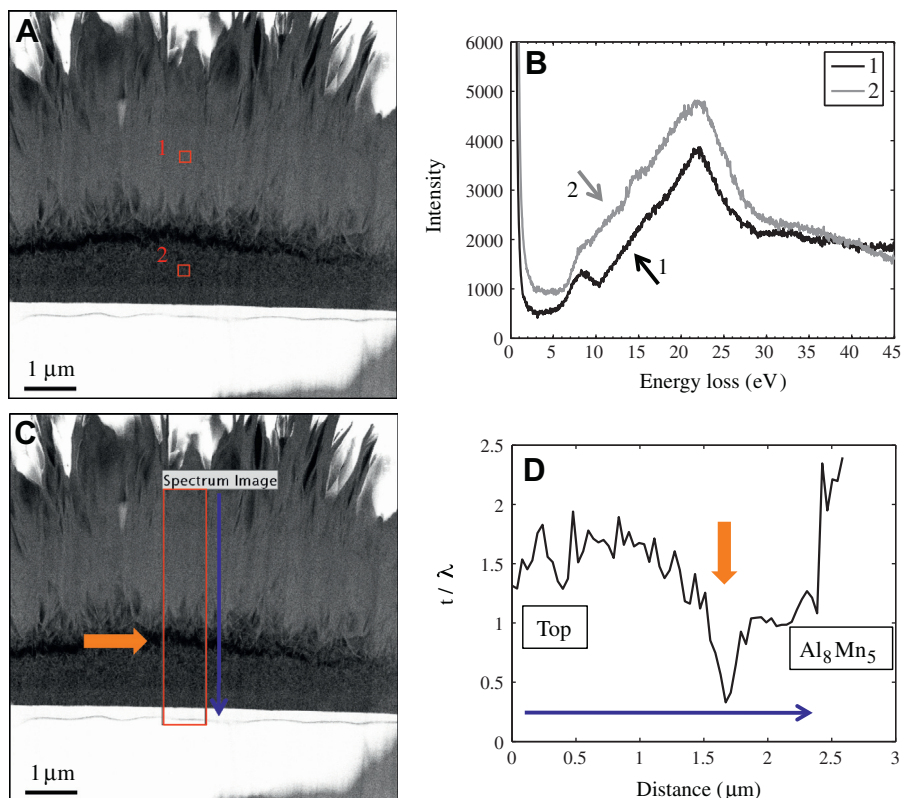
**Fig. 7.** (A) STEM–HAADF micrograph showing the top region of *Sample 96hrs-A*. The low-loss EEL spectra from the two marked locations in (A) are plotted in (B). (C) Same area with the box marking the region used for low-loss spectrum imaging used to map the thickness. (D) Plot of thickness normalized by the inelastic mean free path ($t/\lambda$) versus distance. The blue arrow in (C) shows the direction of the *x*-axis in (D). The arrows in yellow mark roughly the same location as the minimum in the plot in (D). (For interpretation of the references to colour in this figure legend, the reader is referred to the web version of this article.)

2 was recorded on the region between the delaminated layers, and exhibits only the characteristic 22 eV peak for MgO [41] consistent with the diffraction pattern; i.e., SAD #4 in Fig. 10(B). Panel (B), Fig. 11, shows the intensity maps for various energy ranges corresponding to the $Al_8Mn_5$ precipitate plasmon energy range, MgO plasmon peak, and the Mn–$M_{2,3}$ edge. These maps show that MgO is detected between the $Mn_3O_4$ delaminated fragments.

## 4. Discussion

We now focus on consolidating the electron microscopy experimental observations, and approaching them with an electrochemical perspective. We thus refer to the corrosion experimental work previously published in the literature and show that some of the electrochemical observations reported in the literature can be explained at the microstructural level.

A total of four Al–Mn intermetallic particles were examined after periods of either air exposure or aqueous corrosion of alloy AM50. Electron diffraction analyses and XEDS showed these intermetallics to be $Al_8Mn_5$ in all the cases, as expected thermodynamically for cast Mg–Al–Mn alloys close to AM50 in composition [14]. Needle-shaped $Al_8Mn_5$ intermetallics (Figs. 1 and 4) exhibited a crystallographic OR with the Mg matrix, as opposed to intermetallics with more "equiaxed" morphologies.

In the air-exposed surface of the $Al_8Mn_5$ intermetallic (Figs. 2 and 3), relatively high concentrations of Al and O were found, in contrast to the fully immersed specimen on which a distinct Al-depletion of the top layer of the intermetallic was observed (Figs. 6 and 9). The cathodic reaction during Mg corrosion in humid air may differ from that in aqueous solution, since some $O_2$

reduction could accompany water reduction, the ratio of the two reactions depending on the relative humidity. Under aqueous conditions water reduction to $H_2$ is dominant [2,47–49]. Local corrosion damage is evident around the $Al_8Mn_5$ phase, Fig. 2(A), indicating this phase is cathodically active. Jönsson et al. [50] did not observe localized damage close to the Al–Mn phase during atmospheric corrosion of alloy AZ91D, which was attributed to the embedding of this phase in the more corrosion resistant β-$Mg_{17}Al_{12}$ phase. Here, the $Al_8Mn_5$ is within an α-Mg grain (~2–5 wt.% Al in solid solution) and localized attack is observed, as expected given the nobility of this phase compared to α-Mg [15,16]. The higher relative O and Al contents observed at the surface of the air-exposed $Al_8Mn_5$ phase is consistent with the XPS evidence for $Al(OH)_3$ on the surface after corrosion at a pH of ~8.4 [16]. In the case of aqueous corrosion, Figs. 5–11, Al dissolution as a consequence of high local pH values [51] indicates strong cathodic activity on the $Al_8Mn_5$ phase. The lower alkalinity achieved in the air-exposed case suggests the presence of atmospheric $CO_2$ and the formation of magnesium hydroxy carbonate species [24], which can lower the kinetics of anodic dissolution of the Mg matrix.

Of the two Al–Mn precipitates characterized (after 96 h of immersion), one had the corrosion product dome attached (*Sample 96hrs-A*) and the other (*Sample 96hrs-B*) did not. In the latter case, the top region of the precipitate exhibited regions of fractured sections of $Mn_3O_4$, whereas on the specimen with an existing dome of corrosion products, the surface layer adjacent to the precipitate was devoid of Al and early stages of fracturing or disintegration was also evident. The attached corrosion product dome was comprised of an inner layer of MgO and an outer section of large $Mg(OH)_2$ crystals. Enrichment in Al and O, observed on the air ex-
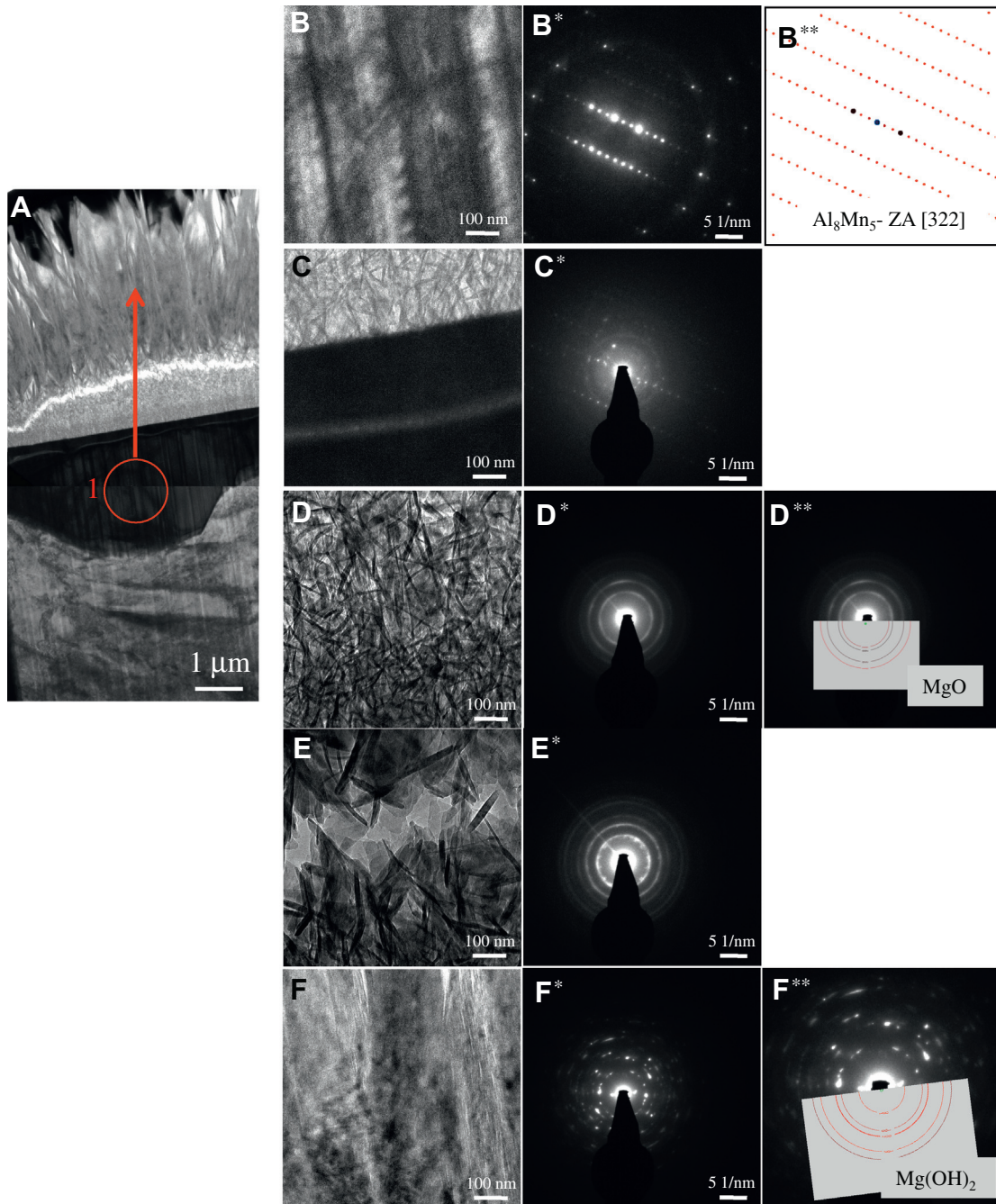
**Fig. 8.** (A) TEM-BF micrograph of *Sample 96hrs-A*. The circle shows the starting position for the SAD data presented in other sections. On the right side of panel (A), the first column shows the BF micrograph from the area of interest (no asterisk). The second column presents the SAD patterns corresponding to each locations (*). The third column shows the simulation of the SAD, where necessary (**).

posed intermetallic particle, was not detected in any of the two regions. XEDS measurements in both cases showed the presence of Al in the corrosion layer, immediately above the $Al_8Mn_5$ intermetallic phase.

These observations suggest that *Sample 96hrs-A* (with corrosion product) demonstrates the early stages of corrosion around an Al–Mn precipitate while *Sample 96hrs-B* (with no corrosion product) captures the later stages. The presence of a thick layer of $Mg(OH)_2$ (*Sample 96hrs-A*) is evidence for a high rate of hydrogen evolution at this location in accordance with reported electrochemical measurements [15,16], identifying Al–Mn intermetallics as the most noble of the common phases in Mg–Al–Mn alloys. The catho-

dic reaction during aqueous corrosion is the reduction of water [2,47]:

$$2H_2O + 2e^- \rightarrow H_2(g) + 2OH^-(aq) \tag{1}$$
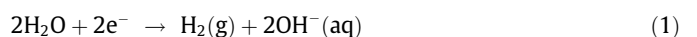
which leads to the precipitation of $Mg(OH)_2$, the equilibrium phase,

$$Mg^{2+}(aq) + 2OH^-(aq) \rightarrow Mg(OH)_2(s) \tag{2}$$
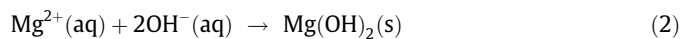
with $Mg^{2+}$ produced anodically [52]. The occurrence of the inner MgO layer, beneath the $Mg(OH)_2$ dome (Figs. 7 and 8), may result from a lower activity of $Mg^{2+}$ ions in close vicinity of the $Al_8Mn_5$ intermetallic phase.
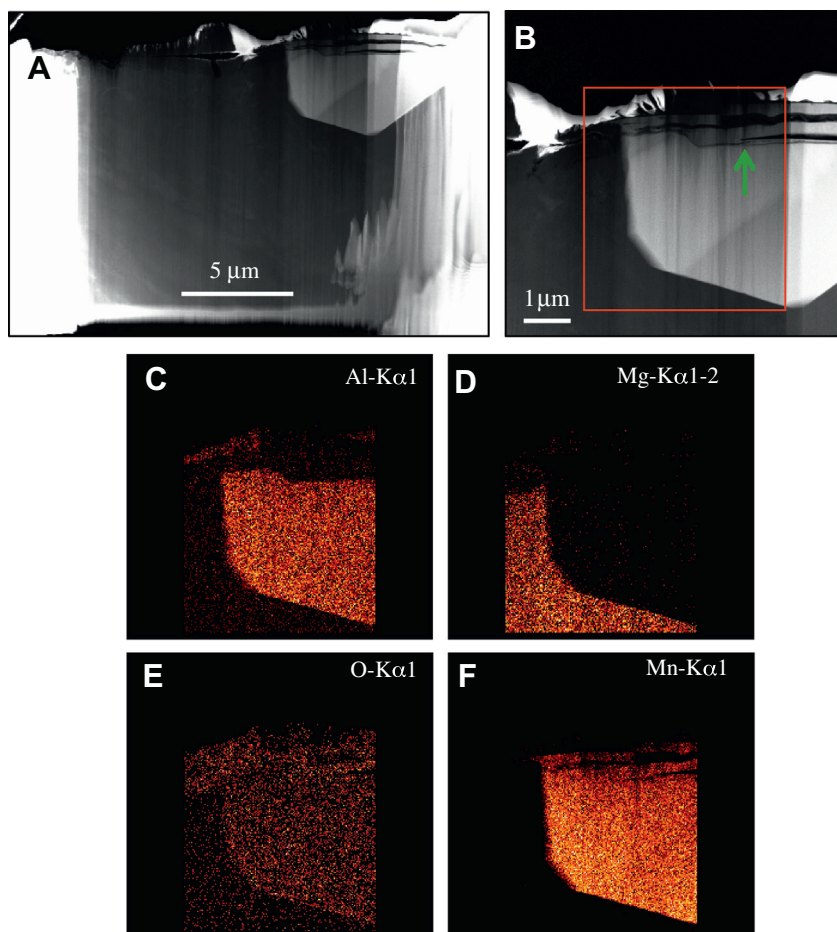
**Fig. 9.** (A) Low magnification STEM–HAADF image of *Sample 96hrs-B*. (B) Higher magnification, with the area used for XEDS mapping with the box. XEDS elemental maps: (C) Al, (D) Mg, (E) O, and (F) Mn. Bright area at the top in (A and B) are the W protective layer, with the intermetallic appearing bright due to the larger average atomic number compared to the Mg matrix. Bright bands at the left and right in panel (A) are due to the larger thickness of the sample.

A local increase in pH would also account for the preferential dissolution of Al, most likely as $AlO_2^-$ [51], from the Al–Mn precipitate. This reaction takes place on the surface of the precipitate, where $H_2$ evolution is at a maximum, and as observed on *Sample 96hrs-B* (Fig. 10), $Mn_3O_4$ is left behind on the top layer. According to the Mn potential-pH equilibrium diagram [51], $Mn_3O_4$ is the most likely oxide in the pH range from 10.5 to 11.5, and its presence is a further indication of high alkalinity in the vicinity of the cathodic $Al_8Mn_5$ phase. A similar "dealloying" of Al–Mn precipitates in a basic solution (NaOH) has been utilized to form nanocrystalline $Mn_3O_4$ [53]. The transition from $Al_8Mn_5$ to $Mn_3O_4$ via a dealloying process would be accompanied by a volume change. For pure $Al_8Mn_5$ (assuming it contains no Fe or Si in solid solution) the unit cell volume normalized to the number of Mn atoms is 36.53 $Å^3$/atom [9], compared to a volume of 28.53 $Å^3$/atom for $Mn_3O_4$ [46]. This volume mismatch would be expected to lead to stress accumulation, and eventually, the fracture of the top surface layer, as observed here for *Sample 96hrs-B*.

This transformation from $Al_8Mn_5$ to $Mn_3O_4$ would be expected to gradually reduce the cathodic activity of the intermetallic phase. This agrees with the more negative corrosion potentials reported for $Al_8Mn_5$ intermetallic in an alkaline NaCl solution (saturated with $Mg(OH)_2$, pH = 10.3, $E_{corr}$ = −0.97 $V_{SHE}$), compared to a neutral pH solution (pH = 6.7, $E_{corr} \sim$ −0.48 $V_{SHE}$) [15]. This can also explain the progressively smaller area-averaged anodic and cathodic current density values, reported by Williams et al. [34], on alloy AZ31 by gradually increasing the pH of the NaCl solution. There, the authors demonstrate that the localized corrosion of AZ31 is cathodically controlled, and a high population of Al–Mn intermetallic particles was stipulated to be the source of the cathodic activation [34] (similar to the proposed role of the cathodic Fe contamination for commercially pure Mg [54]). The ultimate delamination and fracture in the $Mn_3O_4$ oxide layer, as described above, would result in the detachment of the corrosion product dome and eventually the $Mn_3O_4$ layer itself from the alloy surface. This could then expose a fresh surface of the $Al_8Mn_5$ intermetallic to the electrolyte and render it once again an active cathodic site.

## 5. Conclusion

The cathodic activities of the $Al_8Mn_5$ intermetallic particles during the corrosion of sand-cast AM50 alloy in laboratory air and fully immersed in 1.6 wt.% NaCl solution were characterized using site-specific analytical electron microscopy. The top layer of the air-exposed $Al_8Mn_5$ was associated with higher Al and O contents, whereas in the immersed cases preferential dissolution of Al was detected. Neighbouring the $Al_8Mn_5$ precipitates in the immersed samples, we observed a substantial accumulation of corrosion products in the shape of a protruding dome-like feature. This dome consists of an inner section of crystalline MgO and an outer layer of crystalline $Mg(OH)_2$. The Al depletion in the immersed samples, a consequence of high local pH values, leads also to the formation
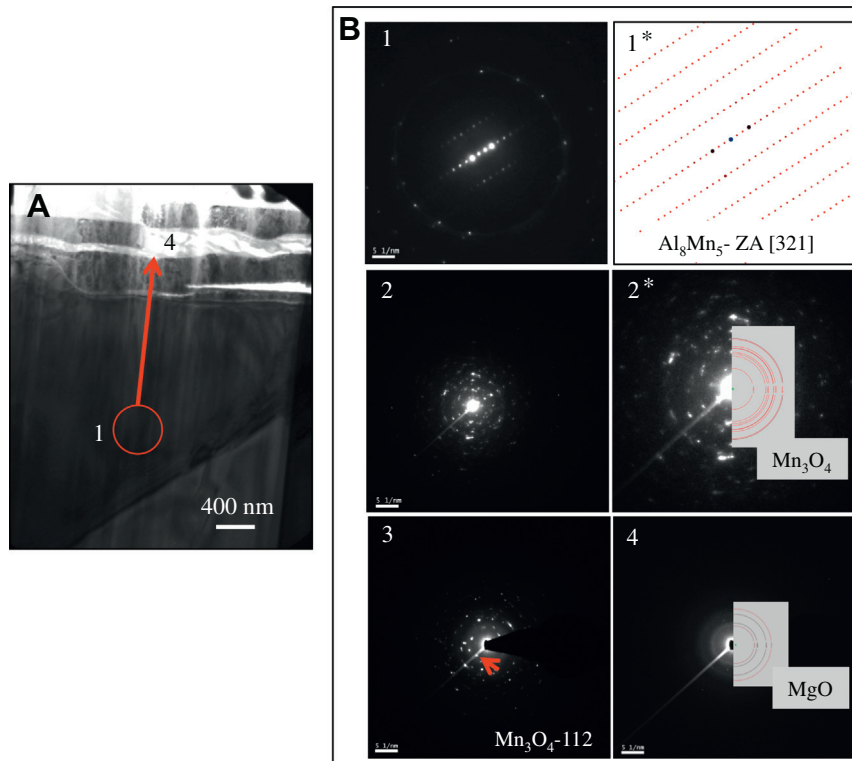
**Fig. 10.** (A) TEM-BF micrograph of *Sample 96hrs-B*. The circle shows the position of the beam for SAD #1, and the arrow depicts the direction of movement for the subsequent SAD patterns. (B) Series of SAD patterns acquired from marked locations in (A). #1* Is the simulation of the spot pattern in 1. #2* Shows details of 2 with the simulation of $Mn_3O_4$ ring pattern. Simulation of the MgO ring pattern is included in SAD #4.
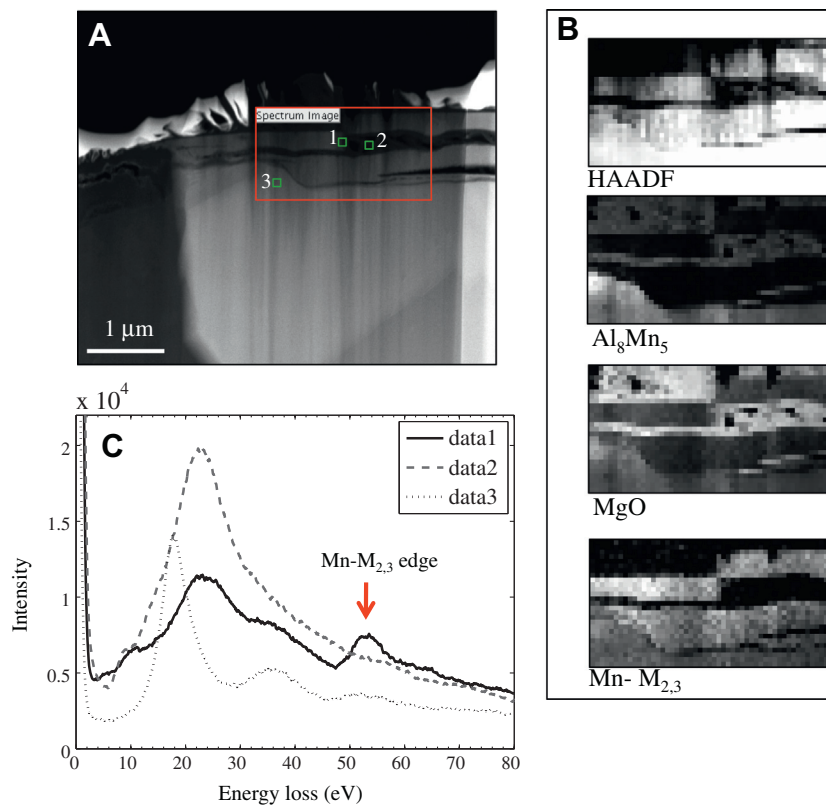


**Fig. 11.** (A) STEM–HAADF image of *Sample 96hrs-B*. The red box marks the region used for spectrum imaging. (B) From top to bottom: the HAADF signal, intensity map corresponding to the $Al_8Mn_5$ precipitate plasmon peak (15.1–20.6 eV), map of MgO plasmon intensity (18.2–26.1 eV), and finally intensity map of the Mn–$M_{2,3}$ edge (48.3–65.4 eV). (C) Three EEL spectra corresponding to the marked three locations in (A). (For interpretation of the references to colour in this figure legend, the reader is referred to the web version of this article.)

of an interlayer of $Mn_3O_4$, between the corrosion product dome and the $Al_8Mn_5$ intermetallic. The air-exposed intermetallic experiences a lower level of alkalinity due to lower rates of anodic dissolution of Mg.

## Acknowledgements

## Appendix A. Supplementary material

Supplementary data associated with this article can be found, in the online version, at http://dx.doi.org/10.1016/j.corsci.2014.02.030.

## References

[1] P. Kurze, Corrosion and surface protections, in: Magnesium Technology, Springer, Berlin, Heidelberg, 2006, pp. 431–497.

[2] E. Ghali, W. Dietzel, K.-U. Kainer, General and localized corrosion of magnesium alloys: a critical review, J. Mater. Eng. Perform. 13 (2004) 7–23.

[3] O. Lunder, J.H. Nordien, K. Nisancioglu, Corrosion resistance of cast Mg–Al alloys, Corros. Rev. 15 (1997) 439–469.

[4] N. Birbilis, M.A. Easton, A.D. Sudholz, S.M. Zhu, M.A. Gibson, On the corrosion of binary magnesium-rare earth alloys, Corros. Sci. 51 (2009) 683–689.

[5] A.D. Südholz, N.T. Kirkland, R.G. Buchheit, N. Birbilis, Electrochemical properties of intermetallic phases and common impurity elements in magnesium alloys, Electrochem. Solid-State Lett. 14 (2011) C5–C7.

[6] H. Matsubara, Y. Ichige, K. Fujita, H. Nishiyama, K. Hodouchi, Effect of impurity Fe on corrosion behavior of AM50 and AM60 magnesium alloys, Corros. Sci. 66 (2013) 203–210.

[7] E.F. Emley, Principles of Magnesium Technology, Elsevier Science & Technology, 1966.

[8] M. Pekguleryuz, Melting, alloying and refining, in: H.E. Friedrich, B.L. Mordike (Eds.), Magnesium Technology, Springer, Berlin, Heidelberg, 2006, pp. 109–143.

[9] M.-X. Zhang, P.M. Kelly, M. Qian, J.A. Taylor, Crystallography of grain refinement in Mg–Al based alloys, Acta Mater. 53 (2005) 3261–3270.

[10] P. Cao, M. Qian, D.H. StJohn, Effect of manganese on grain refinement of Mg–Al based alloys, Scripta Mater. 54 (2006) 1853–1858.

[11] Y. Wang, M. Xia, Z. Fan, X. Zhou, G.E. Thompson, The effect of $Al_8Mn_5$ intermetallic particles on grain size of as-cast Mg–Al–Zn AZ91D alloy, Intermetallics 18 (2010) 1683–1689.

[12] T.B. Massalski, J.L. Murray, L.H. Bennett, H. Baker, Binary alloy phase diagrams, American Society for Metals, Metals Park, Ohio, 1986.

[13] C. Simensen, B. Oberlander, J. Svalestuen, A. Thorvaldsen, Determination of the equilibrium phases in molten Mg-4 wt-Percent Al–Mn Alloys, Z. Metallk. 79 (1988) 537–540.

[14] A. Shukla, A.D. Pelton, Thermodynamic assessment of the Al–Mn and Mg–Al–Mn systems, J. Phase Equilib. Diffus. 30 (2009) 28–39.

[15] M. Jönsson, D. Thierry, N. LeBozec, The influence of microstructure on the corrosion behaviour of AZ91D studied by scanning Kelvin probe force microscopy and scanning Kelvin probe, Corros. Sci. 48 (2006) 1193–1208.

[16] S. Mathieu, C. Rapin, J. Steinmetz, P. Steinmetz, A corrosion study of the main constituent phases of AZ91 magnesium alloys, Corros. Sci. 45 (2003) 2741–2755.

[17] M.C. Merino, A. Pardo, R. Arrabal, S. Merino, P. Casajús, M. Mohedano, Influence of chloride ion concentration and temperature on the corrosion of Mg–Al alloys in salt fog, Corros. Sci. 52 (2010) 1696–1704.

[18] G.L. Song, A. Atrens, Corrosion mechanisms of magnesium alloys, Adv. Eng. Mater. 1 (1999) 11–33.

[19] G. Song, A. Atrens, M. Dargusch, Influence of microstructure on the corrosion of diecast AZ91D, Corros. Sci. 41 (1998) 249–273.

[20] M.-C. Zhao, M. Liu, G. Song, A. Atrens, Influence of the β-phase morphology on the corrosion of the Mg alloy AZ91, Corros. Sci. 50 (2008) 1939–1953.

[21] H. Krawiec, S. Stanek, V. Vignal, J. Lelito, J.S. Suchy, The use of microcapillary techniques to study the corrosion resistance of AZ91 magnesium alloy at the microscale, Corros. Sci. 53 (2011) 3108–3113.

[22] A. Pardo, M.C. Merino, A.E. Coy, F. Viejo, R. Arrabal, S. Feliú Jr., Influence of microstructure and composition on the corrosion behaviour of Mg/Al alloys in chloride media, Electrochim. Acta 53 (2008) 7890–7902.

[23] A. Pardo, M.C. Merino, A.E. Coy, R. Arrabal, F. Viejo, E. Matykina, Corrosion behaviour of magnesium/aluminium alloys in 3.5 wt.% NaCl, Corros. Sci. 50 (2008) 823–834.

[24] R. Lindström, J.-E. Svensson, L.-G. Johansson, The Influence of carbon dioxide on the atmospheric corrosion of some magnesium alloys in the presence of NaCl, J. Electrochem. Soc. 149 (2002) B103–B107.

[25] S. Feliu Jr., A. Pardo, M.C. Merino, A.E. Coy, F. Viejo, R. Arrabal, Correlation between the surface chemistry and the atmospheric corrosion of AZ31, AZ80 and AZ91D magnesium alloys, Appl. Surf. Sci. 255 (2009) 4102–4108.

[26] G.L. Makar, J. Kruger, Corrosion studies of rapidly solidified magnesium alloys, J. Electrochem. Soc. 137 (1990) 414–421.

[27] G. Song, A.L. Bowles, D.H. StJohn, Corrosion resistance of aged die cast magnesium alloy AZ91D, Mater. Sci. Eng.: A 366 (2004) 74–86.

[28] S.J. Splinter, N. McIntyre, The initial interaction of water vapour with Mg–Al alloy surfaces at room temperature, Surf. Sci. 314 (1994) 157–171.

[29] L. Wang, T. Shinohara, B.-P. Zhang, XPS study of the surface chemistry on AZ31 and AZ91 magnesium alloys in dilute NaCl solution, Appl. Surf. Sci. 256 (2010) 5807–5812.

[30] S. Feliu Jr, M.C. Merino, R. Arrabal, A.E. Coy, E. Matykina, XPS study of the effect of aluminium on the atmospheric corrosion of the AZ31 magnesium alloy, Surf. Interface Anal. 41 (2009) 143–150.

[31] J.H. Nordlien, K. NişancioǦu, S. Ono, N. Masuko, Morphology and structure of oxide films formed on MgAl alloys by exposure to air and water, J. Electrochem. Soc. 143 (1996) 2564–2572.

[32] M. Danaie, R.M. Asmussen, P. Jakupi, D.W. Shoesmith, G.A. Botton, The role of aluminum distribution on the local corrosion resistance of the microstructure in a sand-cast AM50 alloy, Corros. Sci. 77 (2013) 151–163.

[33] R.M. Asmussen, P. Jakupi, M. Danaie, G.A. Botton, D.W. Shoesmith, Tracking the corrosion of magnesium sand cast AM50 alloy in chloride environments, Corros. Sci. 75 (2013) 114–122.

[34] G. Williams, H. ap Llwyd Dafydd, R. Grace, The localised corrosion of Mg alloy AZ31 in chloride containing electrolyte studied by a scanning vibrating electrode technique, Electrochim. Acta 109 (2013) 489–501.

[35] B02 Committee, Practice for Codification of Certain Nonferrous Metals and Alloys, Cast and Wrought, ASTM International, 2013.

[36] J.F. King, Technology of magnesium and magnesium alloys, in: H.E. Friedrich, B.L. Mordike (Eds.), Magnesium Technology, Springer, Berlin, Heidelberg, 2006, pp. 219–430.

[37] P. Villars, L.D. Calvert, Pearson's Handbook of Crystallographic Data for Intermetallic Phases, second ed., ASTM International, 1991.

[38] G. Pettersen, E. Øvrelid, G. Tranell, J. Fenstad, H. Gjestland, Characterisation of the surface films formed on molten magnesium in different protective atmospheres, Mater. Sci. Eng.: A 332 (2002) 285–294.

[39] J.-R. Liu, H.-K. Chen, L. Zhao, W.-D. Huang, Oxidation behaviour of molten magnesium and AZ91D magnesium alloy in 1,1,1,2-tetrafluoroethane/air atmospheres, Corros. Sci. 51 (2009) 129–134.

[40] D.A. Porter, Phase Transformations in Metals and Alloys, Van Nostrand Reinhold, 1981.

[41] C.C. Ahn, Transmission electron energy loss spectrometry in materials science and the EELS atlas, John Wiley & Sons, 2006.

[42] D. Su, N. Jiang, J.C.H. Spence, F. He, W.T. Petuskey, On the dehydration mechanism of $Mg(OH)_2$ by a high-energy electron beam, J. Appl. Phys. 104 (2008) 063514–063514-4.

[43] R.F. Egerton, Plasmon energies and inelastic mean free paths, in: Electron Energy-Loss Spectroscopy in the Electron Microscope, Springer, US, 2011, pp. 419–422.

[44] M. Catti, G. Ferraris, S. Hull, A. Pavese, Static compression and H disorder in brucite, $Mg(OH)_2$, to 11 GPa: a powder neutron diffraction study, Phys. Chem. Miner. 22 (1995) 200–206.

[45] M. Cooper, K. Robinson, The crystal structure of the ternary alloy α(AlMnSi), Acta Crystallogr. 20 (1966) 614–617.

[46] D. Jarosch, Crystal structure refinement and reflectance measurements of hausmannite, $Mn_3O_4$, Mineral. Petrol. 37 (1987) 15–23.

[47] N.D. Tomashov, Theory of Corrosion and Protection of Metals: The Science of Corrosion, Macmillan, 1966.

[48] R. Arrabal, E. Matykina, A. Pardo, M.C. Merino, K. Paucar, M. Mohedano, et al., Corrosion behaviour of AZ91D and AM50 magnesium alloys with Nd and Gd additions in humid environments, Corros. Sci. 55 (2012) 351–362.

[49] M. Jönsson, D. Persson, C. Leygraf, Atmospheric corrosion of field-exposed magnesium alloy AZ91D, Corros. Sci. 50 (2008) 1406–1413.

[50] M. Jönsson, D. Persson, R. Gubner, The initial steps of atmospheric corrosion on magnesium alloy AZ91D, J. Electrochem. Soc. 154 (2007) C684–C691.

[51] M. Pourbaix, Atlas of Electrochemical Equilibria in Aqueous Solutions, 2d English ed., National Association of Corrosion Engineers, 1974.

[52] G. Song, A. Atrens, Understanding magnesium corrosion—a framework for improved alloy performance, Adv. Eng. Mater. 5 (2003) 837–858.

[53] C. Xu, R. Wang, Y. Zhang, Y. Ding, A general corrosion route to nanostructured metal oxides, Nanoscale 2 (2010) 906.

[54] G. Williams, H.N. McMurray, Localized corrosion of magnesium in chloride-containing electrolyte studied by a scanning vibrating electrode technique, J. Electrochem. Soc. 155 (2008) C340–C349.